

Location of the bow shock ahead of cloud G2 at the Galactic Center

Aleksander Sądowski¹, Ramesh Narayan¹, Lorenzo Sironi^{1,2} and Feryal Özel^{1,3*}

¹ *Harvard-Smithsonian Center for Astrophysics, 60 Garden St., Cambridge, MA 02138, USA*

² *NASA Einstein Postdoctoral Fellow*

³ *University of Arizona, 933 N. Cherry Avenue, Tucson, AZ 85721, USA*

26 November 2021

ABSTRACT

We perform detailed magnetohydrodynamic simulations of the gas cloud G2 interacting with the accretion flow around the Galactic Center black hole Sgr A*. We take as our initial conditions a steady-state, converged solution of the accretion flow obtained earlier using the general-relativistic magnetohydrodynamic code HARM. Using the observed parameters for the cloud’s orbit, we compute the interaction of the cloud with the ambient gas and identify the shock structure that forms ahead of the cloud. We show that for many configurations, the cloud front crosses orbit pericenter 7 to 9 months earlier than the center-of-mass.

Key words: accretion, accretion disks, black hole physics, relativity, acceleration of particles, radiation mechanisms: non-thermal

1 INTRODUCTION

Gillessen et al. (2012, 2013) discovered an object, likely a cloud of molecular gas, called G2 that is approaching the Galactic Center on a highly eccentric orbit. The center-of-mass of the cloud is expected to reach pericenter, located at radius $R \approx 3.0 \times 10^{15}$ cm from the supermassive black hole Sagittarius A* (Sgr A*), at $t_0 = 2013.69$ (September 2013)¹. During this encounter, the cloud will move supersonically through the hot accretion flow around Sgr A* (Sądowski et al. 2013b) and a bow shock will form ahead of it (Narayan et al. 2012a). The shock provides suitable conditions for particle acceleration and is likely to accelerate hot ambient electrons to relativistic energies.

Narayan et al. (2012a) and Sądowski et al. (2013b) estimated the efficiency of this acceleration and calculated the expected radio synchrotron emission. Depending on model parameters, they predicted radio fluxes $\sim 1 - 20$ Jy at $\nu = 1.4$ GHz. In addition, using simplified assumptions, Sądowski et al. (2013b) estimated that the bow shock will cross pericenter roughly 5 months before the center-of-mass does, and that the peak radio flux will be reached roughly a month later. However, their estimate did not take into account the structure of the cloud or the details of the dynamical interactions between the cloud and the ambient gas, both of which

have the potential to change the shock properties and the expected radio signals.

In this paper we obtain a more reliable estimate of the shock location and the interaction epoch by carrying out general relativistic magnetohydrodynamic (GRMHD) simulations of G2 moving through the turbulent hot accretion flow around Sgr A*. The simulations are performed with the GRMHD code HARM (Gammie et al. 2003) using a realistic model of the accretion flow (Narayan et al. 2012b). The cloud is scaled down to fit within the converged region of the disk simulation. Although the spatial resolution of the simulations is limited, we are able to determine with reasonable confidence that the bow shock is formed ahead of the cloud, and that it crosses pericenter 7 to 9 months earlier than t_0 . The accompanying radio emission is thus expected to reach peak values in Spring or late Summer 2013 for the Gillessen et al. (2013) and Phifer et al. (2013) orbital models, respectively.

Our simulations are the first that include magnetic fields and propagate the cloud through a turbulent accretion flow in three dimensions (3D), thus probing phenomena that were not explored in previous studies. Burkert et al. (2012) and Schartmann et al. (2012) performed two-dimensional fixed-mesh simulations of the cloud approaching Sgr A* and penetrating an isotropic, smooth, non-magnetized and artificially stabilized atmosphere. Similar assumptions about the background gas were adopted by Anninos et al. (2012) who performed 3D adaptive mesh simulation, which are best suited for resolving instabilities at the cloud surface (however, they still neglected the role of magnetic fields). Finally, Saitoh et al. (2012) used a Smoothed Particle Hydrodynamics (SPH) code to simulate the evolution of the cloud assuming the same model for the ambient gas as the other authors, but allowing the gas to cool through optically-thin radiation.

The structure of the paper is as follows. In Section 2 we dis-

* E-mail: asadowski@cfa.harvard.edu (AS); rnarayan@cfa.harvard.edu (RN); lsironi@cfa.harvard.edu (LS); fozel@email.arizona.edu (FO);

¹ Recently, Phifer et al. (2013) obtained another orbital solution, derived from Br-gamma line astrometry and radial velocity measurements, resulting in a later time of closest approach ($t_0 = 2014.21$, March 2014), slightly closer periastron (3800 vs 4400 R_G), and a longer orbital period (276 vs 198 yrs). In this work we use the orbital parameters derived by Gillessen et al. (2013). Because of the similarity of the orbits the shock parameters and its location with respect to the center-of-mass are expected to be similar.

Discuss the initial conditions for our simulations, in Section 3 we describe the simulation results, and in Section 4 we discuss uncertainties and the optimal strategy for radio observations of the G2 impact.

2 MODEL

2.1 Disk model

The radiatively inefficient accretion flow around Sgr A* has been studied extensively through observations and theoretical investigations. The best available constraints come at large radii from the measurement of the gas density at the Bondi radius, which yields $n_e(R_B) \approx 130 \text{ cm}^{-3}$ (Baganoff et al. 2003), and in the innermost regions, where the mass accretion rate onto the black hole has been estimated to be $\dot{M}_{\text{BH}} \approx 10^{-9} \pm 10^{-8} M_\odot \text{ yr}^{-1}$ (see Yuan et al. 2003; Marrone et al. 2007; Mościbrodzka et al. 2009; Dexter et al. 2010; Shcherbakov et al. 2012; Dibi et al. 2012). Models of the gas density and the electron temperature at these small distances can simultaneously account for the long-wavelength spectrum of the accretion flow, the polarization measurements, and the size of the emitting region at 1.3 mm (see Broderick & Loeb 2005). Less is known directly about the properties of the flow at intermediate radii, where the pericenter of G2’s orbit lies. Psaltis (2012) carried out a comparison of the gas properties obtained at intermediate radii by extrapolating the flow properties inwards from the Bondi radius using the model of Quataert (2004) and outwards from the model of Broderick & Loeb (2005) and found reasonable agreement between these solutions between few $\times 10^2$ to $\sim 10^5 R_G$ where $R_G = GM/c^2$ and M is the mass of the black hole.

Numerical simulations similarly rely on the measurements at small and large radii as anchor points to calculate the properties of the gas throughout the flow. In this paper, we make use of the radiatively inefficient accretion simulation around a non-spinning black hole described in Narayan et al. (2012b), which corresponds to the so-called Magnetically Arrested Disk (MAD, Narayan et al. 2003) regime. The accretion disk was solved on a fixed, horizon-penetrating grid with 264 cells logarithmically spaced in radius, 126 cells roughly uniform in θ and 60 cells uniform in ϕ . It was initialized as an equilibrium torus threaded by seed, single-loop magnetic field (Penna et al. 2012). Magneto-Rotational Instability (MRI) develops, the gas accretes and it brings significant magnetic flux onto the BH. We adopted an ideal equation of state with adiabatic index $\gamma = 5/3$. Fig. 1 shows a typical snapshot of the gas density in the $r\theta$ plane.

Because of the very long duration of this simulation, $t = 2.2 \times 10^5 R_G/c$, the simulated accretion flow is in steady state out to a relatively large radius $\sim 200 R_G$ at the equatorial plane, and to much larger radii at higher latitudes. We normalize the gas density in the simulation such that it is consistent with the measured density at the Bondi radius and, at the same time quantitatively agrees with the expected accretion rate at the BH horizon. Shcherbakov (2013, private communication) have shown that the simulated spectrum based on this model agrees with observed spectrum of Sgr A*. Fitting formulae for the mean properties of the accretion flow are given in Sądowski et al. (2013b). The mass of the disk gas inside the cloud radius of pericenter is roughly $0.1 M_{\text{Earth}}$ and is much smaller than the mass of the cloud $M_{\text{cl}} \approx 3 M_{\text{Earth}}$ (Gillessen et al. 2012).

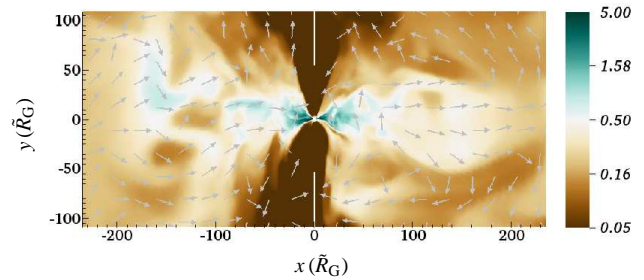


Figure 1. Snapshot of density (arbitrary units) in the $r\theta$ plane for the background model (evolved without the cloud) of the accretion disk taken at the same time as in Fig. 3 (which shows the results of cloud and disk interaction).

2.2 Cloud model

To set up the configuration of the cloud in phase space, which we use as initial conditions for our cloud-disk interaction simulations, we follow the approach described in Gillessen et al. (2012). We start with a spherical cloud of test particles at an earlier epoch corresponding to year 2000.0. We adjust the location and the velocity of the center-of-mass of this initial cloud so that they are consistent with the orbit described in Gillessen et al. (2013). We also assign a spherically symmetric density profile and a distribution of random velocities to the cloud (described in detail in the next paragraph) and adjust these so as to satisfy the distributions of positions and velocities observed in year 2012 (Gillessen et al. 2013). This procedure does not yield a unique model for the initial cloud. Therefore, in addition to the model described in Gillessen et al. (2012), which we refer to as model N1, we consider a number of other models which are all consistent with the data (see Table 1). Our aim is to explore a range of models in order to assess the effect of the initial cloud configuration on the location and properties of the bow shock.

In the alternative models we consider, we model the density profile and the velocity distribution using two parametrizations for the former and three for the latter. For the initial density profile (year 2000), we consider a *Gaussian* distribution, with two values of the full width at half maximum (FWHM), and a constant density cloud (called *flat*), with three choices of the outer radius R_{out} (Table 1). For the *Gaussian* density model, we truncate the cloud at a radius equal to 2σ , where σ is for the standard deviation. For the velocity distribution, we take: 1. a Gaussian distribution with FWHM = 120 km s^{-1} as in Gillessen et al. 2012 (called *normal*), 2. a distribution where the magnitude of the additional velocity component is proportional to the distance from the center-of-mass, with a velocity of 120 km s^{-1} at FWHM or R_{out} for *Gaussian* and *flat* models, respectively (called *scaled*), and 3. a model with no velocity dispersion, where all the particles in the cloud move with the same velocity as the center-of-mass (called *no*). We give in Table 1 the details corresponding to all the models we have considered. Each of these models, when propagated forward from year 2000 to year 2012, gives a cloud of particles with positions and velocities that are consistent with observations.

2.3 Initial MHD setup

The GRMHD simulation that we use to model the background accretion flow (Narayan et al. 2012b) has achieved steady state out to a radius $R \sim 200 R_G$ at the equatorial plane, whereas the cloud orbit has a pericentric radius of $4400 R_G$. To evolve the cloud-disk system

numerically we need to either extrapolate the disk model to several thousand R_G or scale down the cloud and its orbit to $\sim 100R_G$. We choose to do the latter since it allows us to retain the full 3D turbulent structure of the simulated disk.

We scale all distances down by a factor $X = 40$, which brings the pericenter of the orbit down to $R = 110R_G$. This choice, although “ad hoc”, ensures that, on the one hand, the cloud fits within the converged region of the simulation and, on the other hand, it does not go too close to the black hole, where the disk model is no longer self-similar (see Sądowski et al. 2013b). We scale the cloud size, orbit semi-major axis, and other relevant distances by a factor of X^{-1} , the orbital velocity by $X^{1/2}$, and the time relative to pericenter by $X^{-3/2}$. The gas density in the simulation varies with radius as R^{-1} (Sądowski et al. 2013b). Therefore, we scale the cloud density also by X^{-1} .

The strength of the expected bow shock depends on its Mach number — the ratio of the relative cloud-disk velocity to the disk sound speed. The relative velocity increases proportional to the orbital velocities, i.e., by $X^{1/2}$. The temperature in the numerical model follows X^1 and therefore the speed of sound scales as $X^{1/2}$. As a result, the shock strength is independent of the adopted value of the scaling factor X .

We report all simulation results in length units of $\tilde{R}_G = XGM_{SgrA^*}/c^2$, though when reporting times, e.g., in the Tables, we convert back to the parameters of the original G2 cloud.

As the initial conditions for the disk, we choose the final configuration at time $t = 2.2 \times 10^5 R_G/c$ of the ADAF/MAD run described in Narayan et al. (2012b). Then, for each of the cloud models shown in Table 1, we evolve the test particles forward along geodesics up to time $t_{\text{mhd}} = 2012.5$ (except for one model, N0F, where we choose time $t_{\text{mhd}} = 2012.0$; see below). We transfer the mass and momentum corresponding to each test particle to the corresponding grid cell in the simulation, thereby adding the cloud density and momentum to the pre-existing accretion gas in that cell. We assume that the cloud gas is cold (this is certainly true relative to the $> 10^8$ K ambient gas in the accretion disk) and unmagnetized. Thus, the pressure and magnetic field retain the same values as in the original GRMHD simulation. Starting from this initial state (Fig. 2), we run the simulation forward in time and study the motion of the cloud as well as its interactions with the medium.

We ran additional models to test the effects of the initial setup on our results. We ran model N0F with a start time of 2012.0 and confirmed that selecting a start time of 2012.5 vs. this earlier time does not modify the results. In order to assess the impact of the ambient magnetic field on the cloud motion, we also ran one model (N0B) which is identical to the fiducial model N0 except for a magnetic field strength that we set equal to zero. We will discuss the results of this latter run in the later sections.

2.4 Orbit orientation

The GRMHD simulation of the background accretion disk covers the whole domain of (r, θ, ϕ) and has sufficient resolution (264 grid cells in r , 126 in θ , 60 in ϕ) to capture the physics of the dominant MRI modes. The cloud, however, has a relatively small extent compared to the full domain. Therefore, the simulations we describe here have only modest resolution on the scale of the cloud; in particular, our resolution is coarser than other simulations of G2 described in the literature (Anninos et al. 2012; Schartmann et al. 2012; Saitoh et al. 2012).

The primary effect of the numerical diffusion associated with the coarse resolution in the simulations is under resolving Kelvin-

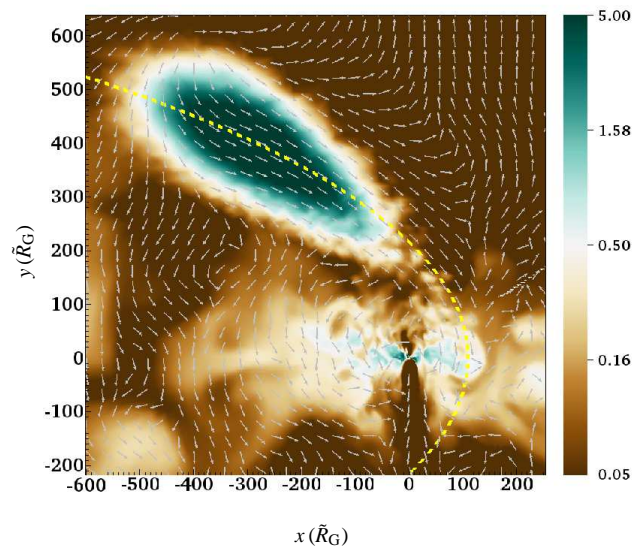


Figure 2. Snapshot of the gas density (arbitrary units) in the $r\theta$ plane for the initial state of the N0 model corresponding to $t = 2012.5$. The dashed yellow line shows the orbit of the cloud center-of-mass.

Helmholtz instabilities at the cloud surface. On the other hand, the presence of magnetic fields in the external medium is expected to dampen the Kelvin-Helmholtz instability (Markevitch & Vikhlinin 2007). Therefore, the potential effects of this instability will be less significant in the present problem and in a realistic disk.

We choose an orbit orientation that allows us to utilize the highest possible resolution to resolve the shocks that develop in the cloud-disk interaction. We assume that (i) the orbital plane of the cloud is highly inclined (inclination angle $i = 60$ deg) with respect to the equatorial plane of the accretion flow, (ii) pericenter is in the equatorial plane (argument of periaapsis $\omega = 0$, corresponding to a single disk crossing, see Sądowski et al. 2013b), and (iii) the cloud and the disk gas counter-rotate with respect to each other. This ensures that the shock normal at pericenter is nearly along the θ direction, where the simulations have the highest resolution. As we show in the next section, the setup we use is sufficient to reasonably resolve the bow-shock region. For comparison, we also consider models with a co-rotating orbit (model N0C), two low-inclination models (N0LN and N0LC) and a model with $\omega = \pi/2$ (double disk crossing, N0D). Parameters of all the models are listed in Table 1.

3 RESULTS

3.1 Physical quantities near the cloud front

We performed 12 simulations and studied in detail the flow structure as the cloud front sweeps past pericenter. In Fig. 3 we show orbital plane snapshots of density, temperature, and magnetic pressure for two representative models, N0 and F0, at a time when the shock has reached the orbit pericenter. In both models the cloud orbit is inclined at an angle $i = 60$ deg and crosses the disk equatorial plane once ($\omega = 0$). Colors in each panel denote the magnitude of the relevant quantity in arbitrary units, vectors show the velocity field, yellow dashed lines show the nominal orbit of the cloud’s center-of-mass, and dashed vertical lines perpendicular to the cloud

Table 1. Cloud models

Model name	Density profile	Size	Velocity dispersion	t_{MHD}	Inclination i	Argument of periapsis ω	Rotation	Magnetic field	Relative time of shock pericenter
N0	Gaussian	FWHM= 3×10^{15} cm	scaled	2012.5	$\pi/3$	0	counter-	on	-0.63
N1	Gaussian	FWHM= 3×10^{15} cm	normal	2012.5	$\pi/3$	0	counter-	on	-0.68
N2	Gaussian	FWHM= 4.5×10^{15} cm	no	2012.5	$\pi/3$	0	counter-	on	-0.82
F0	Flat	$R_{\text{out}} = 2.5 \times 10^{15}$ cm	no	2012.5	$\pi/3$	0	counter-	on	-0.63
F1	Flat	$R_{\text{out}} = 1.5 \times 10^{15}$ cm	scaled	2012.5	$\pi/3$	0	counter-	on	-0.65
F2	Flat	$R_{\text{out}} = 3.5 \times 10^{15}$ cm	no	2012.5	$\pi/3$	0	counter-	on	-0.92
NOF	Gaussian	FWHM= 3×10^{15} cm	scaled	2012.0	$\pi/3$	0	counter-	on	-0.60
NOC	Gaussian	FWHM= 3×10^{15} cm	scaled	2012.5	$-\pi/3$	0	co-	on	-0.66
NOLN	Gaussian	FWHM= 3×10^{15} cm	scaled	2012.5	$\pi/6$	0	counter-	on	-0.54
NOLC	Gaussian	FWHM= 3×10^{15} cm	scaled	2012.5	$-\pi/6$	0	co-	on	-0.61
NOD	Gaussian	FWHM= 3×10^{15} cm	scaled	2012.0	$\pi/3$	$\pi/2$	counter-	on	-0.54
NOB	Gaussian	FWHM= 3×10^{15} cm	scaled	2012.5	$\pi/3$	0	counter- -rotating	off	-0.70

t_{MHD} is the epoch when the corresponding MHD simulation starts. The epoch of shock pericenter is given with respect to the center-of-mass pericenter crossing.

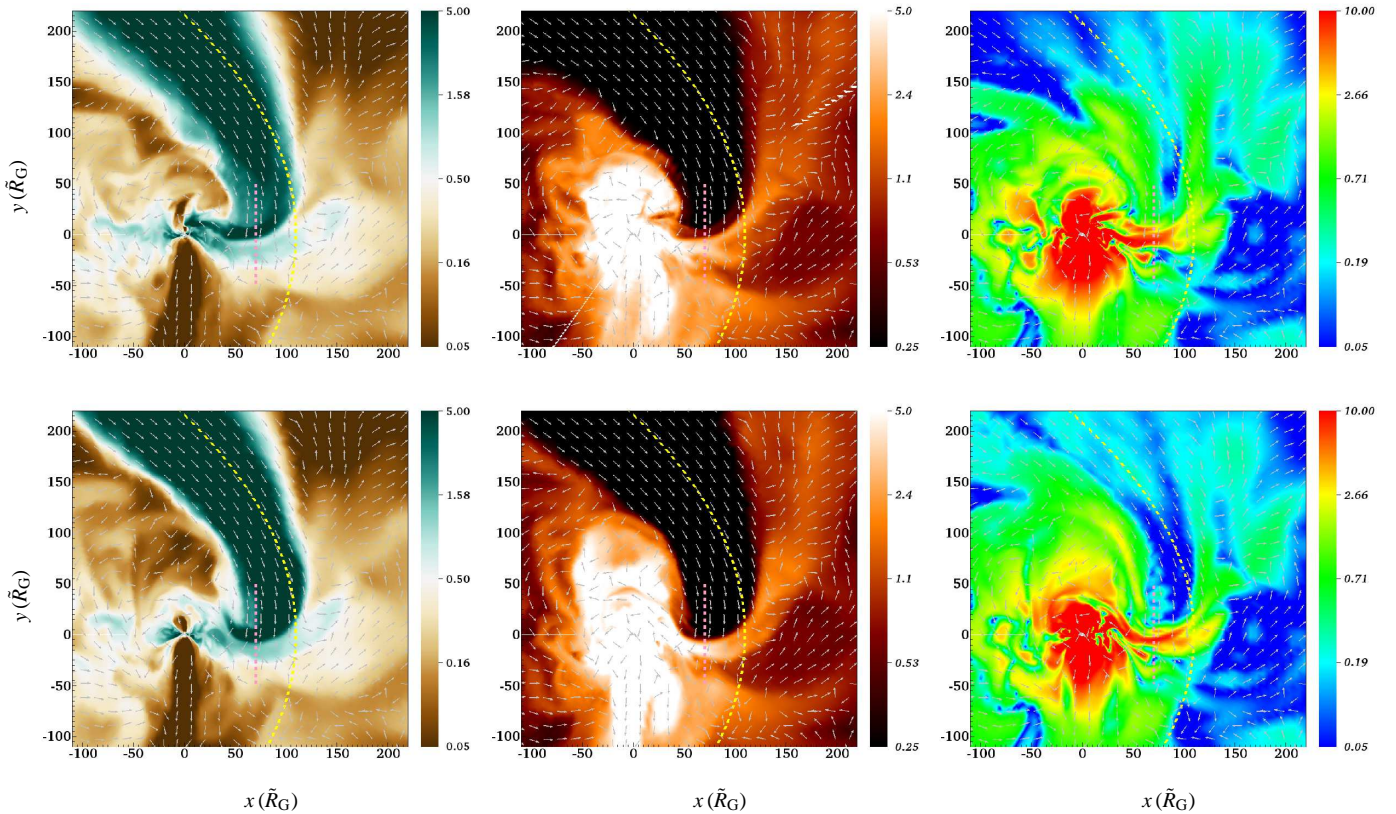


Figure 3. Profiles of density (left), temperature (middle) and magnetic pressure (right panel) on the cloud orbital plane at $t = t_0 - 0.63\text{yr}$ for model N0 (top) and F0 (bottom). Vectors show the velocity field. The yellow dashed line is the cloud center-of-mass orbit while the vertical lines show the cut used to extract profiles across the shock shown in Fig. 4, 6, and 7.

front show the line along which profiles of various quantities are extracted and plotted in Figs. 4, 6, and 7.

The left panels in Fig. 3 show the distribution of density in these snapshots. The cloud has a large density and momentum relative to the ambient gas in the accretion disk, allowing it to plow through the accretion disk easily. However, the tidally stretched front of the cloud is less massive in comparison and experiences hydrodynamic and magnetic drag from the ambient gas. This interaction sculpts the front of the cloud into an oblate shape. We can dis-

tinguish four distinct regions in the structure, which from bottom to top are as follows: (i) undisturbed turbulent disk gas at the bottom (white and brown shades, compare with Fig. 1), (ii) denser shocked disk gas above (light blue) which has been processed through the forward bow-shock which separates these two zones, (iii) high density shocked cloud gas further up (black) which is separated from the shocked external gas by a contact discontinuity, and (iv) unshocked cloud gas which lies above the reverse shock.

The front of the bow-shock is not aligned with the orbit of

the cloud center-of-mass, but lies at a substantially smaller radius, $R = 60\tilde{R}_G$ instead of $R = 110\tilde{R}_G$. This is because of two effects. First, given the initial shape and velocity distribution of the cloud, the parts of the cloud that reach pericenter first are those that have less angular momentum and hence pericenters closer to the black hole. Second, the interaction between the front layers of the cloud and the disk gas causes some additional loss of angular momentum in the cloud material². The effective area of the forward bow-shock is approximately $A = \pi R_{\text{front}}^2$, with $R_{\text{front}} \approx 40\tilde{R}_G = 10^{15}\text{cm}$. This is consistent with the area assumed in Sądowski et al. (2013b).

The middle panels of Fig. 3 show the distribution of temperature. The four zones previously mentioned can also be distinguished in the temperature maps. As expected, the external gas is hot, the shocked external gas is even hotter, the shocked cloud gas is warm, while the unshocked cloud gas is cold. The shape of the bow-shock is most clearly seen in the bottom panel.

The right two panels show the distribution of magnetic pressure. As the magnetized external gas passes through the forward shock, the perpendicular (to the relative velocity vector) field is amplified by compression. This field then drapes around the contact discontinuity and contributes substantially to the total pressure in this region of the shocked gas. This strong field likely also inhibits Kelvin-Helmholtz instability at the contact discontinuity interface (Markevitch & Vikhlinin 2007).

Fig. 4 shows in greater detail the one-dimensional profiles of various quantities of interest along the vertical dashed lines in Fig 3 for models N0 (top) and F0 (bottom). The three dotted lines in the figure show the approximate locations of the forward shock (FS), contact discontinuity (CD) and reverse shock (RS). As can be seen, the shocks are not well resolved, both because the native resolution of the simulation is somewhat low and because the trajectory under consideration crosses the numerical grid at an angle in the $\theta\phi$ plane. Nevertheless, the basic features of the jumps across FS, CD and RS are clearly present. Across the FS, the density (green curve) jumps from its unshocked value up by a factor of a few, as do the temperature (orange) and total pressure (dark blue). The gas thermal pressure (thin blue line) dominates the pressure balance around the FS, whereas a region with high magnetic pressure (dashed blue line) is present close to the CD. The magnetic field accumulated here comes from the shock encounter with a region in the accretion flow where the magnetic pressure exceeded the gas pressure (as in the pre-shock region at $\sim 30\tilde{R}_G$ in Fig 4). The jumps across the FS are consistent with a strong shock with Mach number of a few. More precisely, from the density jump ρ_d/ρ_u across the forward shock, we obtain an estimate for the shock Mach number

$$M = \sqrt{\frac{2\rho_d/\rho_u}{\hat{\gamma} + 1 - (\hat{\gamma} - 1)\rho_d/\rho_u}} \approx 2.5 - 3.0 \quad (1)$$

where $\hat{\gamma} = 5/3$ is the adiabatic index. Alternatively, from the jump p_d/p_u in the gas thermal pressure (which dominates the pressure

² The simulations we performed do not allow us to study the impact of the cloud on the BH mass accretion rate. It is expected that most of the additional accreted material would come from "filaments" stripped from the cloud surface. Yet, we likely underestimate this effect because of poor resolution. Furthermore, the innermost region of our simulation domain is not self-similar (see Section 2.3) and therefore after scaling it up it will not reproduce the real Sgr A* accretion disk at the corresponding radii. Thus, any estimate of the cloud mass deposited at these radii is likely to be unreliable.

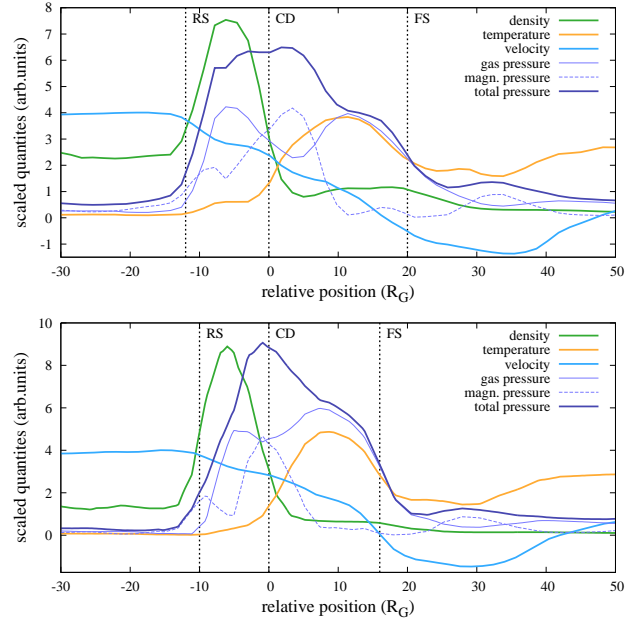


Figure 4. Profiles of density, temperature, velocity, gas pressure, magnetic pressure, and total pressure across the shock for models N0 (top) and F0 (bottom) at $t = t_0 - 0.63\text{yr}$. The cloud front is moving to the right. The vertical dotted lines show approximate locations of the reverse shock (RS), contact discontinuity (CD) and forward shock (FS).

balance in the vicinity of the forward shock, see Fig. 4), we derive

$$M = \sqrt{\frac{(\hat{\gamma} + 1)p_d/p_u + \hat{\gamma} - 1}{2\hat{\gamma}}} \approx 2 - 2.5 \quad (2)$$

Both estimates concur to suggest a moderate value for the shock Mach number at pericenter, $M \sim 2 - 3$, in agreement with the assumptions of Sądowski et al. (2013b). However, it is possible that we slightly underestimate the shock strength because of the limited resolution and the resulting numerical diffusion.

There are somewhat larger jumps across the RS, which has a larger Mach number since the unshocked cloud gas is very cold. In particular, the density of the shocked gas (between the RS and the CD) is quite large. As expected, the pressure is continuous across the CD, and correspondingly the density and the temperature have inversely related jumps.

The cyan curve shows the longitudinal velocity along the cut. The velocity goes from that of the external gas to that of the cloud in two jumps, one each at FS and RS. In addition, between the shocks and the CD, there is a gradient in the velocity, which we discuss next.

While the profiles described above are qualitatively consistent with the expectations for a planar FS–CD–RS double-shock system, the full structure we have at hand is indeed a three-dimensional bow-shock. This introduces some important differences, caused by the fact that, in a bow-shock, gas can flow to the side and slide away along the contact discontinuity (Landau & Lifshitz 1959). In order to understand the differences specific to this geometry, we used the numerical code KORAL (Sądowski et al. 2013a) to simulate a toy hydrodynamical problem in which a solid spherical object plows through a homogeneous hot fluid with a relative Mach number $M = 2.5$.

Fig. 5 shows the results from this hydrodynamic simulation after the system has reached steady state. Because we assume a

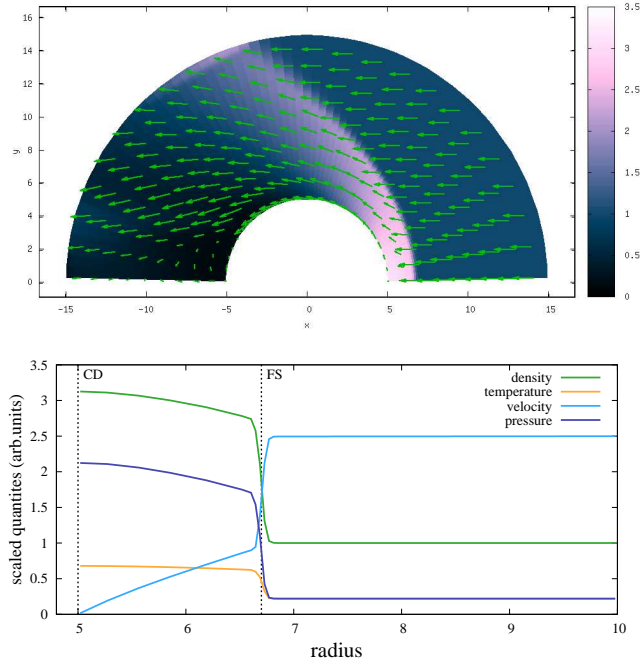


Figure 5. Top: Density profile and the velocity field in a toy three-dimensional bow shock simulation with $\mathcal{M} = 2.5$ in spherical coordinates. Bottom: Profiles of density, pressure, temperature and velocity along the impact axis.

rigid sphere, there is no reverse shock, and the surface of the sphere plays the role of the contact discontinuity. The forward bow-shock, however, is very clearly delineated in the top panel. The bottom panel shows profiles of density, pressure, temperature and velocity along the symmetry axis. The jumps in these quantities at the FS are as expected from standard theory of adiabatic shocks. The main differences from the planar shock problem appear in the post-shock gas. Whereas for the planar case we expect all gas properties to be independent of position after the shock, in the bow-shock case we see that the density, temperature and pressure all increase between the FS and the CD, whereas the velocity drops down to zero at the CD. These differences are caused by gas being diverted around the CD, as seen from the velocity vectors in the top panel.

A comparison of the toy model results in Fig. 5 with the G2 simulation results in Fig. 4 indicates that similar variations are present in the latter. The variations in the pressure and velocity, in particular, are quite similar to those seen in the 3D hydrodynamical problem, suggesting that the shock geometry is responsible for the behavior seen in Fig. 5.

To investigate the effects of the magnetic structure of the accretion flow on the cloud-disk encounter, we have run the simulation N0B, without magnetic fields. As compared to our fiducial model N0, we find that the run N0B yields a similar structure for the FS, which is consistent with the fact that pressure balance at the FS is dominated by the gas thermal component (see Fig 4). However, the RS in N0B is weaker than in N0, lacking the magnetic support present for N0 in the vicinity of the CD.

We also study the time evolution of the shock by looking at the shock structure at different snapshots in the simulation. Figs. 6 and 7 show cuts across the FS–CD–RS structure for models N0 and F0, respectively, at four different times. The cloud moves from left to right and the vertical dotted line indicates the location of the disk mid-plane. The various features discussed earlier are clearly seen

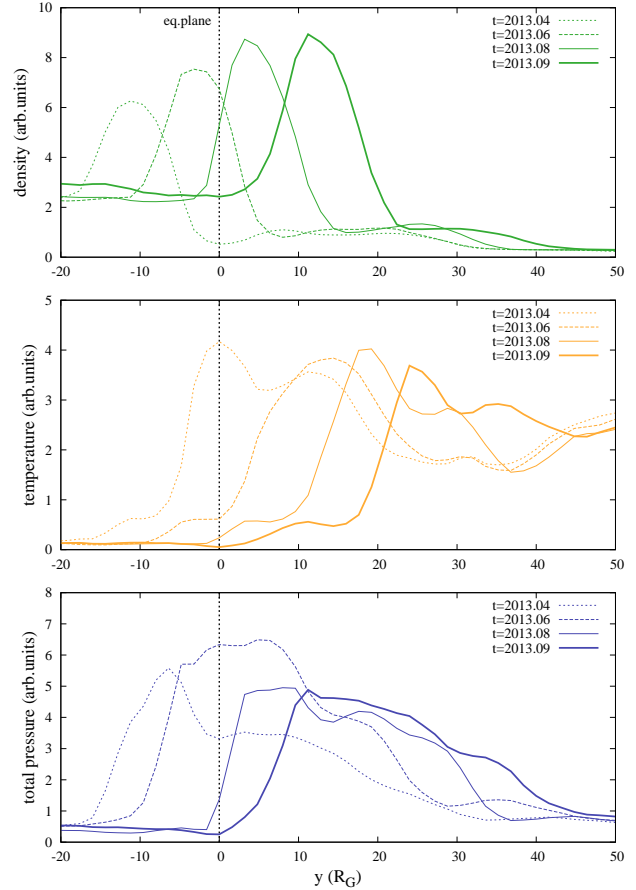


Figure 6. Evolution of density (top), temperature (middle), and total pressure (bottom panel) across the shock with time for model N0. The vertical dotted line shows the location of the disk equatorial plane.

in all the snapshots and the whole pattern moves steadily to the right. In addition, there is evidence for some growth in the amount of shocked gas with increasing time.

3.2 Pericenter crossing times

Sądowski et al. (2013b) calculated synchrotron emission from relativistic electrons accelerated in the bow shock of G2 and showed that the maximum radio synchrotron emission is expected roughly a month after the bow shock crosses pericenter. It is evident from the cloud-disk interaction models we have presented here that the bow shock forms ahead of the front of the cloud, and reaches pericenter well ahead of the pericentric passage of the cloud’s center-of-mass. We list in the last column of Table 1 the times when the cloud front reaches the location corresponding to true anomaly $\theta = 0$ of the center-of-mass orbit in each of our 12 simulations. In most models the crossing occurs 7 to 9 months before the cloud center-of-mass’ epoch of pericenter (t_0). A larger initial cloud size (models N2 and F2) causes the crossing to occur two or three months earlier. On the other hand, clouds on orbits with low inclinations (N0LN and N0LC) or with double crossing (N0D) are slowed down by interaction with the disk gas compared to the fiducial model N0. In these models, the cloud front reaches pericenter roughly a month later. Model N0B with no magnetic fields shows an early crossing time by about a month, indicating that drag due to the magnetic field

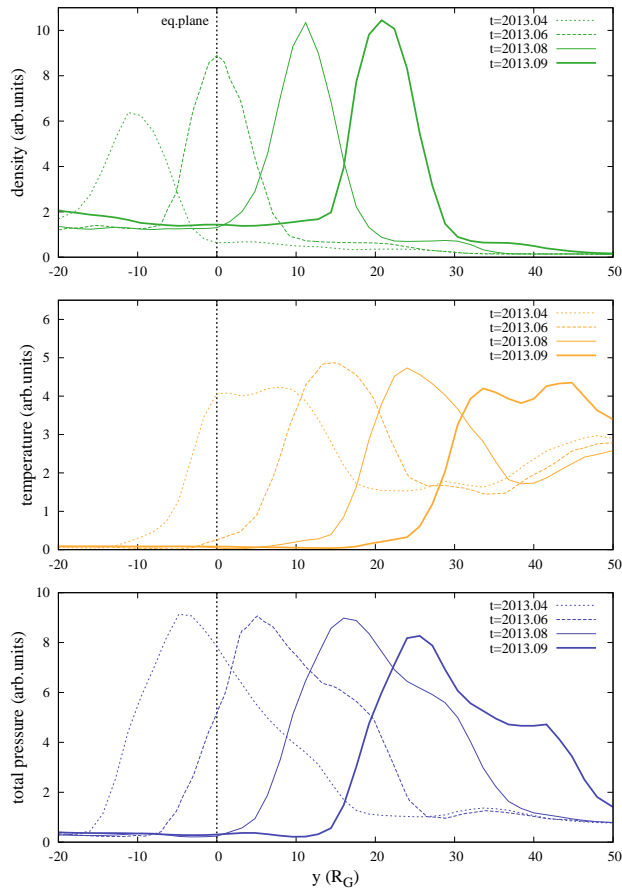


Figure 7. Similar to Fig. 6 but for model F0.

draped around the CD plays a dynamically significant role in all the other models.

4 DISCUSSION

In this paper, we performed detailed magnetohydrodynamic simulations of the interaction between the gas cloud G2 and the accretion flow around the Galactic Center black hole Sgr A*. We scaled down the cloud to fit it within the converged region of previously simulated accretion flow model solved on a fixed numerical grid. Despite the limited numerical resolution we were able to simulate the formation of the bow-shock region and qualitatively study its properties. We showed that for any reasonable cloud structure and orbit orientation that fit the current data, the shock pericenter crossing takes place approximately 7 to 9 months earlier than the epoch when the cloud center-of-mass reaches pericenter. Depending on the orbital model, we predict the peak radio emission in Spring 2013 for Gillessen et al. (2013) or late Summer 2013 for Phifer et al. (2013) orbit solutions, respectively.

The Very Large Array (VLA) carried out observations of the Galactic center during October 2012, December 2012, February 2013, and March 2013 as part of a monitoring campaign.³ The data taken in February and March provide only upper limits to the flux

³ Data are publicly available at <https://science.nrao.edu/science/service-observing>.

from Sgr A* at low frequencies because the VLA was in the low-resolution D-configuration during this observation and could not fully disentangle the fluxes of Sgr A* from that of other nearby sources. Intriguingly, the flux at 14 GHz, which suffers less from source confusion, shows a modest flux increase, which could be due to the extra radio emission from the bow shock or due to intrinsic variability of the source. Another observation was made by Kassim et al. (2013) using the Giant Metrewave Radio Telescope (GMRT) in late January and early February 2013 and resulted in non-detection of sub-GHz emission.

February and March monitoring observations did not show a brightening but there are recent reports of brightening at 22GHz and 32 GHz (Brunthaler et al. 2013; Tsuboi et al. 2013). It remains to be seen whether this flux enhancement is due to the bow shock.

We encourage continued monitoring of the Galactic Center in the very near future. Higher resolution observations can not only verify a flux enhancement but may also be able to detect the displacement of the known radio source coincident with the black hole from the bow shock emission $\sim 4400R_G$ away. Finally, observations at higher frequencies, even with the more compact array configurations, could differentiate an intrinsic brightening. Even though we predict the largest flux increase around a GHz, significant enhancement can be observed up to ~ 14 GHz.

5 ACKNOWLEDGEMENTS

A.S. and R.N. were supported in part by NASA grant NNX11AE16G. L.S. is supported by NASA through Einstein Postdoctoral Fellowship grant number PF1-120090 awarded by the Chandra X-ray Center, which is operated by the Smithsonian Astrophysical Observatory for NASA under contract NAS8-03060. F.Ö. acknowledges support from NSF grant AST-1108753 and from the Radcliffe Institute for Advanced Study at Harvard University. The simulations were performed on XSEDE resources under contract No. TG-AST120010, and on NASA High-End Computing (HEC) resources through the NASA Advanced Supercomputing (NAS) Division at Ames Research Center.

REFERENCES

- Anninos, P., Fragile, P. C., Wilson, J., & Murray, S. D. 2012, *Astrophysical Journal*, 759, 132
- Baganoff, F. K., Bautz, M. W., Brandt, W. N., et al. 2001, *Nature*, 413, 45
- Broderick, A. E., & Loeb, A. 2005, *Monthly Notices of the Royal Astronomical Society*, 363, 353
- Broderick, A. E., Fish, V. L., Doeleman, S. S., & Loeb, A. 2011, *Astrophysical Journal*, 735, 110
- Brunthaler A., Falcke F., Bower G. C., Ott J., Reid M. J. 2013, *The Astronomer's Telegram*, 5014, 1
- Burkert, A., Schartmann, M., Alig, C., Gillessen, S., Genzel, R., Fritz, T. K., & Eisenhauer, F. 2012, *Astrophysical Journal*, 750, 58
- Dexter, J., Agol, E., Fragile, P. C., & McKinney, J. C. 2010, *Astrophysical Journal*, 717, 1092
- Dibi, S., Drappeau, S., Fragile, P. C., Markoff, S., & Dexter, J. 2012, *Monthly Notices of the Royal Astronomical Society*, 426, 1928
- Gammie, C. F., McKinney, J. C., & Tóth, G. 2003, *Astrophysical Journal*, 589, 444
- Gillessen, S., Genzel, R., Fritz, T. K., et al. 2012a, *Nature*, 481, 51
- Gillessen, S., Genzel, R., Fritz, T. K., et al. 2013, *Astrophysical Journal*, 763, 78
- Kassim, N. E., Hyman, S. D., Intema, H., Clarke, T. E., & Subrahmanyan, R. 2013, *The Astronomer's Telegram*, 4922, 1

- Landau, L. D., & Lifshitz, E. M. 1959, *Course of theoretical physics*, Oxford: Pergamon Press, 1959,
- Markevitch, M., & Vikhlinin, A. 2007, *Physics Reports*, 443, 1
- Marrone, D. P., Moran, J. M., Zhao, J.-H., & Rao, R. 2007, *Astrophysical Journal Letters*, 654, L57
- Mościbrodzka, M., Gammie, C. F., Dolence, J. C., Shiokawa, H., & Leung, P. K. 2009, *Astrophysical Journal*, 706, 497
- Narayan, R., Igumenshchev, I. V., & Abramowicz, M. A. 2003, *Publications of the Astronomical Society of Japan*, 55, L69
- Narayan, R., Özel, F., & Sironi, L. 2012a, *Astrophysical Journal Letters*, 757, L20
- Narayan, R., Sądowski, A., Penna, R. F., & Kulkarni, A. K. 2012b, *MNRAS*, accepted
- Penna R., Kulkarni A., Narayan R., 2012, Submitted to *Astronomy & Astrophysics*
- Phifer, K., Do, T., Meyer, L., Ghez, A. M., Witzel, G., Yelda, S., Boehle, A., Lu, J. R., Morris, M. R., Becklin, E. E., & Matthews, K. 2013, arXiv:1304.5280
- Psaltis, D. 2012, *Astrophysical Journal*, 759, 130
- Psaltis, D., Narayan, R., & Broderick A. 2013, in preparation
- Saitoh, T. R., Makino, J., Asaki, Y., et al. 2012, arXiv:1212.0349
- Sądowski, A., Narayan, R., Tchekhovskoy, A., & Zhu, Y. 2013a, *Monthly Notices of the Royal Astronomical Society*, 429, 3533
- Sądowski, A., Sironi, L., Abarca, D., et al. 2013b, arXiv:1301.3906
- Schartmann, M., Burkert, A., Alig, C., et al. 2012, *Astrophysical Journal*, 755, 155
- Shcherbakov, R. V., Penna, R. F., & McKinney, J. C. 2012, *Astrophysical Journal*, 755, 133
- Tsuboi, M., Asaki, Y., Yonekura Y., Kaneko H., Miyamoto, Y., Seta M., Nakai N., Kameya, O. et al. 2013, *The Astronomer's Telegram*, 5013, 1
- Yuan, F., Quataert, E., & Narayan, R. 2003, *Astrophysical Journal*, 598, 301